Journal of Catalysis 261 (2009) 66–74

Contents lists available at ScienceDirect

Journal of Catalysis

www.elsevier.com/locate/jcat

Ethanol steam reforming over Co-based catalysts: Role of oxygen mobility

Hua Song, Umit S. Ozkan *

Department of Chemical & Biomolecular Engineering, The Ohio State University Columbus, OH 43210, USA

ARTICLE INFO

Article history:
Received 10 July 2008
Revised 4 November 2008
Accepted 4 November 2008
Available online 2 December 2008

Keywords:
Cobalt catalyst
Zirconia
Ceria
Bio-ethanol steam reforming
Deactivation
Carbon deposition
Carbon nanofiber
Oxygen mobility

ABSTRACT

The effect of oxygen mobility on the bio-ethanol steam reforming of ZrO_2- and CeO_2-supported cobalt catalysts was investigated. The supported catalysts were prepared by incipient wetness impregnation (IWI) and characterized through N_2 physisorption, X-ray photoelectron spectroscopy, temperature programmed oxidation, laser Raman spectroscopy, diffuse reflectance infrared Fourier transform spectroscopy, O_2 pulse chemisorption, isotopic labeling, and transmission electron microscopy techniques at various life stages of the catalyst. The results indicated that the catalyst deactivation was due mostly to deposition of various types of carbon on the surface although cobalt sintering could also be contributing to the deactivation. The addition of ceria was found to improve the catalytic stability as well as activity, primarily due to the higher oxygen mobility of ceria.

1. Introduction

As the wide-spread application of fuel cells becomes closer to reality, increased attention has been focused on hydrogen production technologies. Bio-ethanol steam reforming (BESR) offers an environmentally friendly route for hydrogen production from renewable sources, with potentially little contribution to green house effect, since CO_2 can be recycled through photosynthesis during the plant growth. Bio-ethanol can be obtained from fermentation of biomass (e.g. sugar cane, cellulose, corn). Because of its low toxicity and ease of deliverability, ethanol steam reforming lends itself very well to a distributed-production strategy. Development of a non-precious catalytic system with high activity and stability will be an important step in making this technique economically competitive.

With increased interest in hydrogen as an energy carrier for fuel cells, studies in the literature on ethanol steam reforming catalysts have also increased significantly in recent years. Catalysts utilized are mainly Ni, Cu, Co and supported noble metals, such as Rh, Ru, Re, Pd, Ir and Pt [1–4], which have been reviewed by Haryanto et al. [5] and Vaidya et al. [6]. Although supported noble metal catalysts have been shown to have significant activity in 500–600 °C range and at high space velocities [7–9], high cost of these metals limits their application. As a less expensive alternative, cobalt-based catalysts have been reported to have superior ethanol steam reforming performance due to their high activity for C–C bond cleavage at temperatures as low as 350–400 °C [10–12]. At these temperatures, researchers have reported good selectivity to CO_2 and H_2 with CH_4 being the only by-product.

Catalyst deactivation during BESR has been reported over various catalyst systems [13–16], especially over supported Ni catalysts [17–24]. Furthermore, in most of these studies, the metal sintering and the deposition of carbonaceous species such as amorphous carbon, carbon filament, and carbonate species have been recognized as the main causes of catalyst deactivation. The number of studies examining the activity of supported cobalt catalysts is fewer [25–27], most detailed studies being reported by Llorca and co-workers [11,12,28–32] and the most commonly used support being ZnO.

In recent years, increased attention has been given to the role of oxygen mobility in improving the catalytic stability during BESR through preventing metal particles from sintering [33,34] and suppressing the formation of carbonaceous species by gasification. While most of these studies are focused on the utilization of CeO_2 or ZrO_2–CeO_2 mixed oxide supported noble-metal catalysts [35–37], the importance of a similar phenomenon for non-precious metal catalysts such Co has received much less attention.

In our earlier publications [38,39], we have reported on the catalytic activity of Co/ZrO_2 catalysts in ethanol steam reforming and the effect of synthesis parameters on catalytic performance. In this study, we focus on the deactivation behavior of these Co-based catalysts and the effect of the oxygen mobility of the support on catalytic activity and stability. Ceria, which is known for its high oxygen storage capacity, has been reported to enhance the catalytic activity and stability in several reactions

* Corresponding author.
E-mail address: ozkan.1@osu.edu (U.S. Ozkan).

0021-9517/$ – see front matter
doi:10.1016/j.jcat.2008.11.006

such as CO oxidation, water–gas shift, and steam reforming of methane [40–42]. In this paper, the role of CeO_2 addition in improving the stability of Co-based catalysts, as examined through characterization studies that included N_2 physisorption, X-ray photoelectron spectroscopy (XPS), temperature-programmed oxidation (TPO), laser Raman spectroscopy (LRS), diffuse reflectance infrared Fourier transform spectroscopy (DRIFTS), O_2 pulse chemisorption, $^{16}O_2/^{18}O_2$ exchange, and transmission electron microscopy (TEM) techniques, is reported.

2. Experimental

2.1. Catalysts preparation

Supported cobalt catalysts with 10 wt% metal loading were prepared in air by incipient wetness impregnation from cobalt(II) nitrate hexahydrate (Aldrich 99.999%) aqueous solutions. The pure supports used were ZrO_2 (Saint Gobain, surface area: 55 m^2/g, pore volume: 0.21 cm^3/g) and CeO_2 (powder <5 μm, 99.9% Aldrich, surface area: 71 m^2/g, pore volume: 0.34 cm^3/g). The 10 wt%CeO_2–ZrO_2 support was prepared by impregnating the ZrO_2 support using an aqueous solution of cerium(III) nitrate (Aldrich 99.999%). All the supports were calcined for 3 h in air at 500 °C prior to metal impregnation. After repeating the impregnation of cobalt precursor and drying steps (at 95 °C) as many times as determined by the pore volume of the corresponding supports, the resulting samples were calcined at 400 °C for 3 h in the air and stored for use. The term "fresh sample" is used to represent the sample after calcination; the "reduced sample" denotes the sample reduced at 400 °C for 2 h; and the "spent sample" refers to the sample after reduction treatment and exposure to reaction atmosphere for various time periods.

2.2. Catalysts characterization and reaction performance measurement

The surface areas of the fresh and spent catalysts were measured using nitrogen adsorption at 77 K (Micromeritics ASAP 2010). Before each measurement, the sample was degassed under 130 °C overnight to remove any impurities adsorbed from the atmosphere during storage.

XPS analysis was performed using an AXIS His, 165 Spectrometer manufactured by Kratos Analytical with a monochromatized Al$K\alpha$ X-ray source. 2.3 V voltage was chosen to make the charge balance. A stainless steel sample holder was used. Survey scans were performed to identify all the elements within the sample, followed by more detailed regional scans for Co 2p, C 1s, O 1s, Zr 3d orbitals in order to achieve the high resolution for these elements of interest. A controlled-atmosphere transfer chamber was used for transferring the sample to the XPS instrument without exposure to atmosphere.

Temperature-programmed oxidation (TPO) experiments were performed using Autochem-2920 (Micromeritics) with an online mass spectrometer (MS) (MKS Instruments, 1–300 amu). The samples were first pretreated at 300 °C with He for 30 min in order to remove adsorbed contaminants during storage. After cooling down to room temperature under helium, 10%O_2/He (30 ml/min) was introduced into the reactor and TPO experiments were subsequently performed with a heating rate of 10 °C/min after the MS signal was stable.

Raman spectra were taken with a LabRAM HR-800 spectrometer equipped with an OLYMPUS BX41 microscope (50× magnification) and a CCD detector. An argon ion green laser (514.5 nm, operated at 3 mW) was used as the excitation source during spectra collection.

O_2 pulse chemisorption experiments were conducted using AutoChem II 2920 (Micrometrics) connected with a Cirrus Mass Spectrometer (MKS Instruments, 1–300 amu). Catalysts of ~200 mg were sandwiched between two layers of quartz wool and subjected to an oxidative cleaning step in air for 30 min, at the calcination temperature of the sample, followed by a reduction step at 400 °C for 2 h. After the system was flushed with He to remove any moisture, the O_2 pulses were introduced at 300 °C. The $m/z = 32$ signal was continuously detected by the MS until there was no variation between two consecutive peaks.

$^{16}O_2/^{18}O_2$ exchange experiments were performed using a Thermo Finnegan Trace Ultra DQC GC/MS. ~50 mg samples were placed in a U-tube quartz reactor. Following a cleaning step under He at 400 °C for 30 min to remove impurities adsorbed during storage, the reactor was cooled down to 300 °C, at which temperature the $^{16}O_2/^{18}O_2$ exchange took place. The $m/z = 32$, 34, and 36 (mass-to-charge ratio) signals were monitored by the mass spectrometer during the exchange process. 10% Ar was included in the 2% $^{16}O_2$/He stream to account for the gas-phase hold-up time, as described previously [43–45]. In addition, blank experiments were also performed and showed no exchange in the gas phase when no catalyst was present.

The TEM experiments were performed by using Philips Tecnai TF-20 TEM instrument operated at 200 kV. An X-ray analyzer for EDS is incorporated into the instrument for elemental analysis under STEM mode for improving image contrast between C and Co phases. The sample was first dispersed in ethanol and supported on Lacey-formvar carbon on a 200 mesh Cu grid before the TEM images were recorded.

DRIFTS was performed with a Thermo NICOLET 6700 FTIR spectrometer equipped with a liquid-nitrogen-cooled MCT detector and a KBr beam splitter. The *in situ* experiments were performed using a Smart collector DRIFT environmental chamber with ZnSe windows. Following the pretreatment under He at 400 °C for 30 min and reduction under 5%H_2/He at 400 °C for 2 h, the environmental chamber was heated to 450 °C for 1 h under He for removing moisture generated from the reduction step. The reactant vapors generated from a two-bubbler system were then flowed over the sample for 1 h at room temperature using He as a carrier gas. The sample was then flushed with He for 10 min. Spectra were taken at pre-set intervals while the sample temperature was ramped from 25 to 500 °C.

The catalytic performance measurement and analysis methods used were reported elsewhere [38]. Briefly, all catalysts were first pretreated at 400 °C for 30 min. under He and then reduced *in situ* at 400 °C for 2 h under 5%H_2/He. The reactant liquid consisting of ethanol and water at 1:10 molar ratio was delivered into an evaporator. The generated reactant vapor was carried by He and introduced into the reactor. The dilution ratio varied between 40 and 75 (inert-to-ethanol molar ratio). For neat experiments, gas phase reactants were directly fed to the reactor without dilution with an inert gas. Subsequently the catalytic performances were tested in the temperature range of 300 to 550, in 50 °C increments. The catalyst was held at each temperature for at least 2 h. At the end of the catalytic test, the flow of $EtOH + H_2O$ was stopped and the catalyst was cooled under He stream. The hydrogen yield is defined as H_2 yield % $= \frac{\text{moles of } H_2 \text{ produced}}{6\times(\text{moles of ethanol fed})} \times 100$. The time-on-stream (TOS) tests were performed at 450 °C for different time periods depending on the deactivation rate of various samples. The spent samples after TOS experiments were cooled down to room temperature under helium before characterization.

The turnover frequency (TOF) reported in the paper is calculated based on the ethanol conversion rate divided by the total available metallic cobalt active sites contained over the samples charged in the reactor. The cobalt dispersion is estimated using a H_2 chemisorption technique, which is described in detail previously [38].

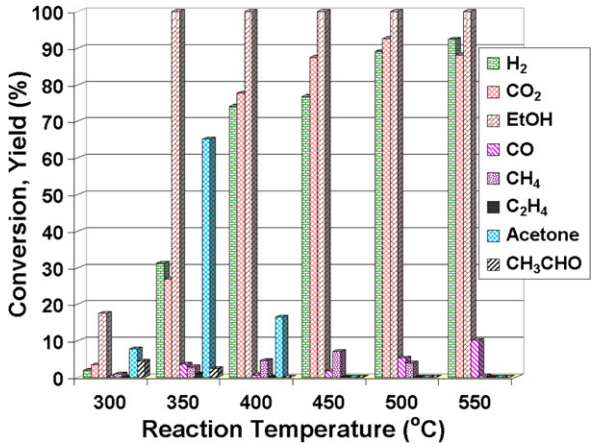

Fig. 1. Variation of ethanol conversion and product yields with temperature during steady-state steam reforming over 10%Co/ZrO_2 (EtOH:H_2O = 1:10 (molar ratio), GHSV = 5000 h^{-1}, and C_{EtOH} = 1.2%).

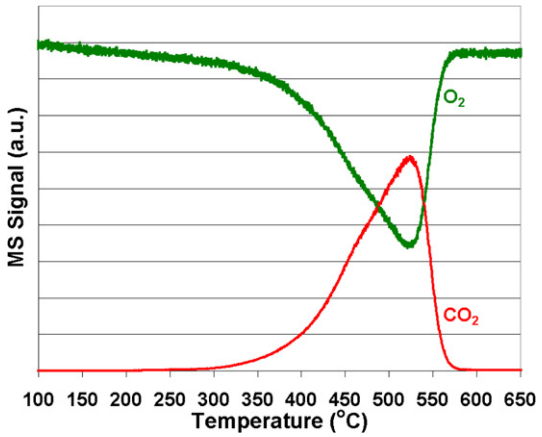

Fig. 2. O_2 ($m/z = 32$) and CO_2 ($m/z = 44$) traces during TPO over spent 10%Co/ZrO_2.

3. Results and discussion

3.1. The deactivation behavior of Co/ZrO_2 catalysts in BESR

As we have reported previously [38], Co/ZrO_2 catalysts with a 10%Co loading gave high H_2 yields, at temperatures as low as 450 °C. The H_2 yield at this temperature is 77% and reaches 92% at 550 °C, which is equivalent to 5.5 mol of H_2 produced per mol of ethanol fed. What is also worth noting in Fig. 1 is that at or above 450 °C, there are no liquid products remaining in the system. At 450 °C and above, the only by products are CO (less than 2%) and CH_4 (less than 7%). At 550 °C, the only H-containing product is H_2, giving it a 100% selectivity. The only other product observed at this temperature besides H_2 and CO_2 is CO. At lower temperatures, in addition to the main products which are expected to be formed during BESR reaction, (i.e., H_2 and CO_2), small quantities of acetone, CO, CH_4, C_2H_4, and acetaldehyde were also observed at different levels. As seen in the figure, above 350 °C, the ethanol conversion is complete, hence the yield of H_2 is determined by the competing reactions, including ethanol decomposition, dehydration, dehydrogenation, methanation, WGS and reverse WGS reactions.

Although the activity and H_2 yield over these Co/ZrO_2 catalysts were quite promising, the TOS experiments showed that after about 25 h on stream at 450 °C, the activity declined rapidly. There was also significant pressure build-up in the reactor.

Post-reaction characterization of the spent 10%Co/ZrO_2 catalysts provided information as to the nature of catalyst deactivation. Fig. 2 shows the results of TPO experiment performed over a deactivated catalyst. As the temperature is raised under an oxygen flow, significant levels of CO_2 formation were observed over the catalyst, indicating that carbon was deposited over the surface during reaction. The maximum in the CO_2 signal, which takes place at 520 °C is accompanied by a minimum in the O_2 signal, showing the oxygen depletion during the oxidation of the carbon deposited on the surface.

The XPS spectra of 10%Co/ZrO_2 were taken at different life stages, i.e., fresh, reduced and spent, which are shown in Fig. 3. The Co $2p_{3/2}$ peak centered at 780.3 eV over fresh sample could be assigned to Co_3O_4. The peak shift to 778.4 eV was observed when the reduced sample was analyzed, indicating the existence of metallic Co [46–49]. Moreover, the absence of the shake-up lines nearby the two main Co 2p peaks characteristic of Co^{2+} [50–52] implied the full reduction of cobalt oxide under these reduction conditions. The spectrum of the spent sample showed a very weak

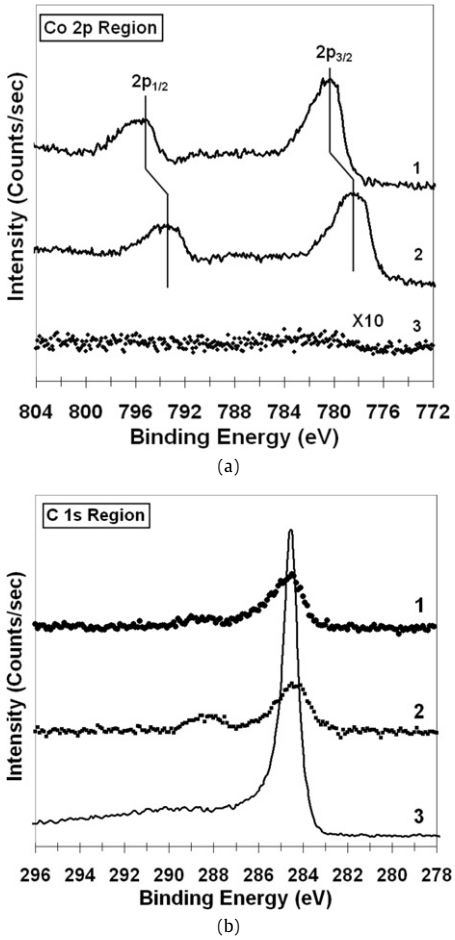

Fig. 3. (a) Co 2p and (b) C 1s region of the X-ray photoelectron spectra of 10%Co/ZrO_2: (1) fresh, (2) reduced, and (3) spent catalyst.

signal in the Co 2p region, suggesting that most of the Co sites were covered by (or encased in) carbon. Fig. 3b shows C 1s region of the XPS spectra of 10%Co/ZrO_2 catalyst taken at different life stages, i.e., fresh, reduced and spent. Compared to the fresh and reduced samples, there was a very strong signal observed over the spent catalyst, indicating carbon deposition on the surface. Zr 2p and O 1s regions of the spectra (not shown) also showed reduced intensities compared to the fresh and reduced samples. However, this was especially severe for the Co 2p signal.

Raman spectroscopy was used to characterize the carbon deposited on the post-reaction catalysts. Fig. 4 shows the Raman

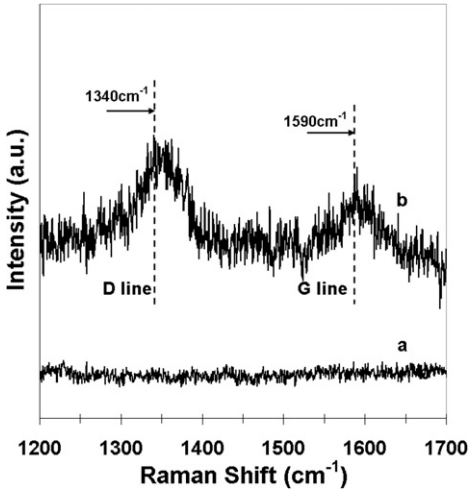

Fig. 4. Raman spectra of 10%Co/ZrO_2 (a) fresh, (b) spent.

spectra taken over 10%Co/ZrO_2 sample, before reaction (reduced) (Fig. 4a) and after 45 h on stream at 450 °C (Fig. 4b). The two broad bands observed over the spent catalyst that are centered at 1340 and 1590 cm^{-1} are characteristic of disordered carbonaceous and ordered graphitic species [28] and are referred as D band and G band, respectively. The G band is known to be very sensitive to the extent of two-dimensional graphitic ordering. The degree of the disordering of the carbonaceous materials can be roughly estimated quantitatively based on the integrated intensity of D and G bands. The larger the microcrystalline planar size L_a defined as $44(I_G/I_D)$ is [53], the higher the degree of ordering is in the carbonaceous materials. In our case, L_a is estimated to be 2.5 nm after peak fitting by using two Gaussian type bands, which is higher than the reported value obtained from carbon deposits over Co-based catalysts [12], indicating the higher degree of ordering.

Fig. 5 shows TEM and STEM images of the Co/ZrO_2 samples at three different life stages—calcined (a), reduced (b) and spent (c–f). The Co_3O_4 crystallites are represented as darker particles (a), while the ZrO_2 supports are seen as lighter particles. The lattice fringes are visible for both phases (i.e., Co_3O_4 and ZrO_2). The average particle size decreased from 24 nm for the Co_3O_4 to 12 nm for Co particles, following a reduction treatment. The decrease in size was confirmed by *in situ*-XRD results as well [40]. For spent samples, in addition to amorphous carbon, carbon nanofibers are also observed over 10%Co/ZrO_2 with varying diameters. The cobalt particles appear to be encased at the tip of the fibers. Figs. 5d and 5f are the STEM images of the same sample area represented in Figs. 5c and 5e, respectively. Superimposed on the STEM images are the EDS analysis results from the highlighted areas. The area highlighted in Fig. 5d is at the tip of a fiber and the analysis shows a very strong Co signal. The area highlighted in Fig. 5f is on a fiber and EDS analysis shows a very strong C signal. The Cu signal observed in both cases is due to the copper grid used to support the samples. The carbon fibers are seen to vary in diameter substantially, depending on the size of the Co particle that catalyzes its growth. While most of the fibers are shorter with diameters around 20 nm, there are some fibers with much larger diameters (~150 nm). Compared to the average size of the Co particles of freshly reduced samples, some of the Co particles encased in carbon fibers appear to be much larger, suggesting that there may have been sintering of Co particles during reaction, resulting in larger particle sizes.

3.2. The effect of support modification with CeO_2 on catalytic performance

While the Co/ZrO_2 catalysts deactivated rapidly due to carbon deposition on the surface, addition of ceria to the support showed significant improvement in catalyst stability. Fig. 6 shows a comparison of the TOS performance of 10%Co/ZrO_2 and 10%Co/10%CeO_2–ZrO_2 catalysts at 450 °C. While the initial activity and hydrogen yields observed over these two catalysts are comparable at 450 °C (~76%), Co/ZrO_2 catalyst shows rapid deactivation after about 30 h of TOS. There was not much change in selectivity during the rapid deactivation. The catalyst that contains 10% CeO_2 in the support maintains its activity even after 110 h TOS. Ceria addition also imparts the catalysts with a higher reforming activity, especially at lower temperatures, as seen in the inset.

The surface areas and pore volume of these two catalysts are compared in fresh and spent form and the results obtained through N_2 physisorption are presented in Table 1. The Co/ZrO_2 catalysts show increased surface area and pore volume after TOS, while ceria-containing sample does not show much change. The increase in surface area and pore volume may be due to carbon deposition on the surface of the Co/ZrO_2 catalyst.

When Co/CeO_2–ZrO_2 catalysts were characterized with LRS after being kept on stream for 110 h, there was no Raman signal that corresponded to carbon (data not shown), indicating that there was either no carbon deposition or the carbon on the surface was below the detection limits of the Raman spectrometer.

Post-reaction TEM characterization of the Co/CeO_2–ZrO_2 catalysts was also performed (Fig. 7). Surface was found to be mostly free of any carbon deposition with very few carbon fibers detected. Co particles appeared to remain intact on the surface. EDS analysis also verified that there was not much carbon deposited on the surface.

Since incorporation of CeO_2 into the zirconia support demonstrated significantly better catalytic performance, Co catalysts supported on CeO_2-only were tested under more demanding reaction conditions (i.e., higher ethanol concentrations and higher GHSV). Fig. 8 shows a comparison of the H_2 yields achieved over 10%Co/10CeO_2–ZrO_2 and 10%Co/CeO_2 catalysts. Under these reaction conditions, Co/ZrO_2 catalysts showed very rapid deactivation and pressure build-up, not allowing data collection at steady-state. As shown in Fig. 8, Co catalysts supported on ceria gave substantially higher yields for H_2 than the ones supported on CeO_2–ZrO_2 supports in the entire temperature range studied.

The three catalysts (Co/ZrO_2, Co/CeO_2–ZrO_2 and Co/CeO_2) were also compared using TOFs calculated from ethanol conversion data at 450 °C. For these measurements, neat reaction conditions were used. The TOF data, which are presented in Table 3, show that the intrinsic activities of the three catalysts increase in the order of Co/ZrO_2 < Co/CeO_2–ZrO_2 < Co/CeO_2.

The long term stability of the three catalysts were tested under neat reaction conditions (without the dilution of an inert gas) with EtOH:H_2O = 1:10 (molar ratio), GHSV = 5000 h^{-1} and C_{EtOH} = ~7.5%. The Co/CeO_2 catalyst was kept on-line at 450 °C for 45 h and showed no change in activity or product distribution. The H_2 yield under these conditions was slightly higher than 60%. The Co/ZrO_2 deactivated within the 1st hour and showed severe pressure build-up. Co/CeO_2–ZrO_2 catalyst showed deactivation starting after ~15 h. These experiments showed that the stability also increased in the order of Co/ZrO_2 < Co/CeO_2–ZrO_2 < Co/CeO_2.

Since Co catalysts supported on ceria or ceria-modified zirconia gave much higher yields and showed much better stability and resistance to coking, the differences between the ceria-containing and ceria-free catalytic systems were examined using different techniques.

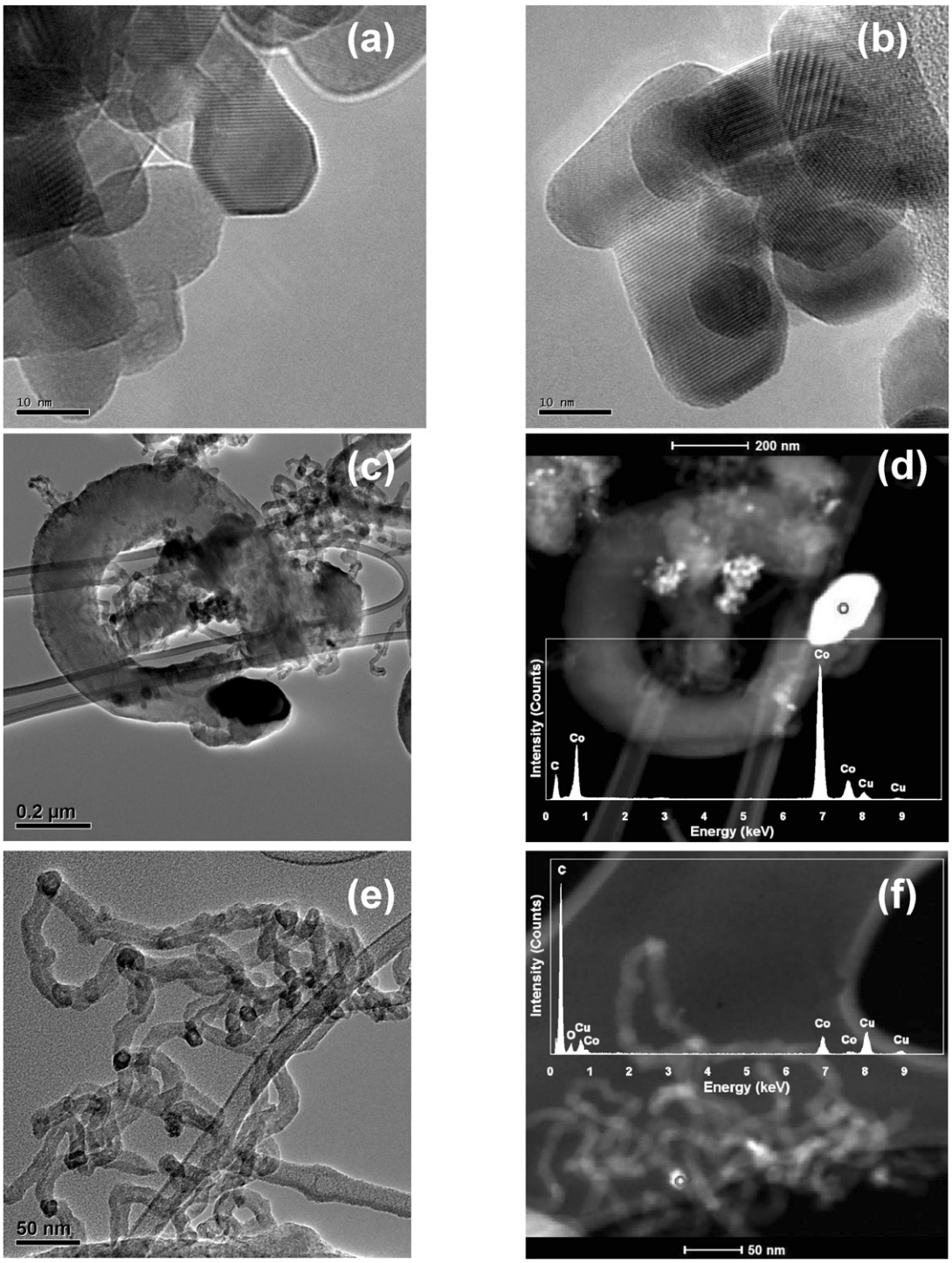

Fig. 5. Electron microscopy of 10%Co/ZrO_2: (a) TEM image after calcination, (b) TEM image after reduction, (c and d) TEM images of spent catalysts, (e and f) STEM images of the same sample areas shown in (c) and (d), respectively. EDS analyses of the highlighted areas are superimposed.

Co crystal sizes were determined using X-ray diffraction. Table 2 summarizes the evolution of cobalt crystal sizes at different life stages for all three catalysts calculated using Scherrer equation. The diffraction lines used for these calculations are (311) and (111) for the Co_3O_4 and Co phases, respectively. All three catalysts show a decrease in crystal size upon reduction. The percent increase in crystal size upon exposure to reaction medium is the largest for Co/ZrO_2 catalyst. Co/CeO_2 catalyst shows no increase in crystal size during reaction.

DRIFTS technique was used to monitor the surface species during BESR reaction over 10%Co/ZrO_2. Fig. 9 a and b show the *in situ* DRIFT spectra taken during ethanol TPD over 10%Co/ZrO_2 and 10%Co/CeO_2, respectively. At room temperature, in the region between 3600–3800 cm^{-1}, the negative features originate from the molecularly adsorbed ethanol through the formation of hydrogen bridge bonding with the OH groups of the support. Furthermore, the molecularly adsorbed ethanol produces the vibrational bands located at 1323 ($\delta(CH_3)$) and 1280 cm^{-1} ($\delta(OH)$) [1]. Ethanol adsorption also leads to the formation of monodentate and bidentate ethoxy species through disassociation as identified by the CH_3 bending (1443, 1381 cm^{-1}) and CCO stretching (1161, 1110, 1066 cm^{-1}) vibrations [29]. The C–H stretching located within

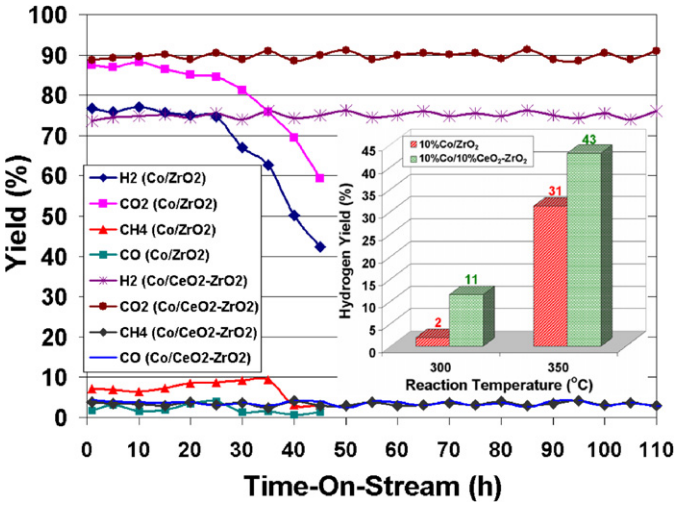

Fig. 6. (a) Product yields obtained over 10%Co/ZrO_2 and 10%Co/10%CeO_2–ZrO_2 during ethanol steam reforming collected at 450 °C (EtOH:H_2O = 1:10 (molar ratio), GHSV = 5000 h^{-1} and C_{EtOH} = 1.2%).

Table 1
Surface area, pore volume and pore size of fresh and spent 10%Co/ZrO_2 and 10%Co/10%CeO_2–ZrO_2 catalysts measured using N_2 physisorption.

Catalyst	Surface area (m^2/g)	Pore volume (cm^3/g)	Pore size (Å)
Co/ZrO_2 Fresh	49.5	0.202	158.0
Co/ZrO_2 Spent	56.4	0.251	170.7
Co/CeO_2–ZrO_2 Fresh	38.2	0.160	160.3
Co/CeO_2–ZrO_2 Spent	38.6	0.163	164.8

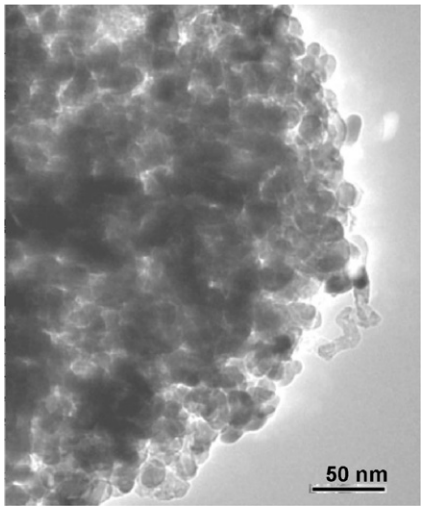

Fig. 7. TEM image taken over spent 10%Co/10%CeO_2–ZrO_2.

3000–2700 cm^{-1} (2970, 2928, 2867, 2710 cm^{-1}) comes from the CH_3– and CH_3CH_2–groups. Initial temperature increase favors the ethoxide species adsorbed in bidentate form (stronger 1161 cm^{-1} peak). The bands characteristic of ethoxy species disappeared with further temperature increase due to oxidation with the lattice oxygen from the support. Surface acetate species were observed to form subsequently at 1552 cm^{-1} (ν_{assym}(COO)), 1441 cm^{-1} (ν_{sym}(COO)), and 1346 cm^{-1} ($\delta(CH_3)$) [54]. These species could first evolve to monodentate carbonate [1,55] as an intermediate, then dissociate into CO_2, which is seen through the bands at 2361 and 2338 cm^{-1}. It was noted that in the region from 2200 to 2000 cm^{-1} where adsorbed CO bands would be [56] there were no peaks during the entire run. Interestingly, over the CeO_2-supported

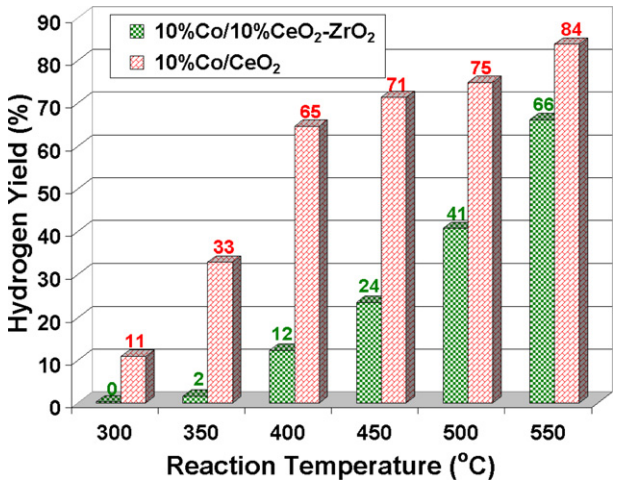

Fig. 8. Comparison of H_2 yields obtained over 10%Co/10%CeO_2–ZrO_2 and 10%Co/CeO_2 (EtOH:H_2O = 1:10 (molar ratio), GHSV = 20,000 h^{-1} and C_{EtOH} = 2%).

Table 2
Cobalt/cobalt oxide crystal size estimation from XRD (nm).

Catalyst	Fresh[a]	Reduced[b]	Spent
Co/ZrO_2	27	15	24
Co/CeO_2–ZrO_2	29	20	25
Co/CeO_2	31	25	25

[a] Calculations are based on (311) diffraction line for Co_3O_4.
[b] Calculations are based on (111) diffraction line for Co.

Table 3
The TOFs (s^{-1}) based on ethanol conversion collected under neat reaction conditions at 450 °C: EtOH:H_2O = 1:10 (molar ratio), GHSV = 5000 h^{-1} and C_{EtOH} = 7.5%.

Co/ZrO_2	0.054
Co/CeO_2–ZrO_2	0.214
Co/CeO_2	0.476

catalyst, the appearance and disappearance of each surface species mentioned above occur at much lower temperatures (shown in Fig. 9b). For instance, even at room temperature, the vibration peaks characteristic for acetate species are present, implying the abundance of oxygen on the surface available for oxidation of adsorbed ethanol species. The fact that almost no species remain on the surface of ceria-supported sample at 400 °C while very strong acetate bands are still visible even at 500 °C over the ZrO_2-supported catalyst is an indication that the oxidation of surface species is easily facilitated due to the oxygen mobility of the ceria support. This observation is consistent with the resistance to coking seen over the ceria-containing catalysts.

The *in situ* DRIFT spectra obtained during ethanol/water TPD over 10%Co/ZrO_2 and 10%Co/10%CeO_2–ZrO_2 are shown in Fig. 10. Compared to Fig. 9a, the spectra collected during ethanol/water TPD spectra over Co–ZrO_2 at room temperature shows much stronger adsorption bands around 3600–3800 cm^{-1} due to adsorbed water. The peak located around 1653 cm^{-1} [56] is also due to the O–H scissoring resulting from adsorbed water. As a result of water dilution, the vibration peaks corresponding to the molecular or dissociative adsorption of ethanol are much weaker than the ethanol TPD spectra taken at the same temperature. Many of the same features are observed as those seen in Fig. 9a, except for slight shifts. The effect of water addition to facilitate ethanol conversion can be seen from the disappearance of the surface acetate species peaks at lower temperatures. It is worth noting that similar phenomena are observed over CeO_2 containing catalyst, however, the increased accessibility of oxygen and hence the ease of oxida-

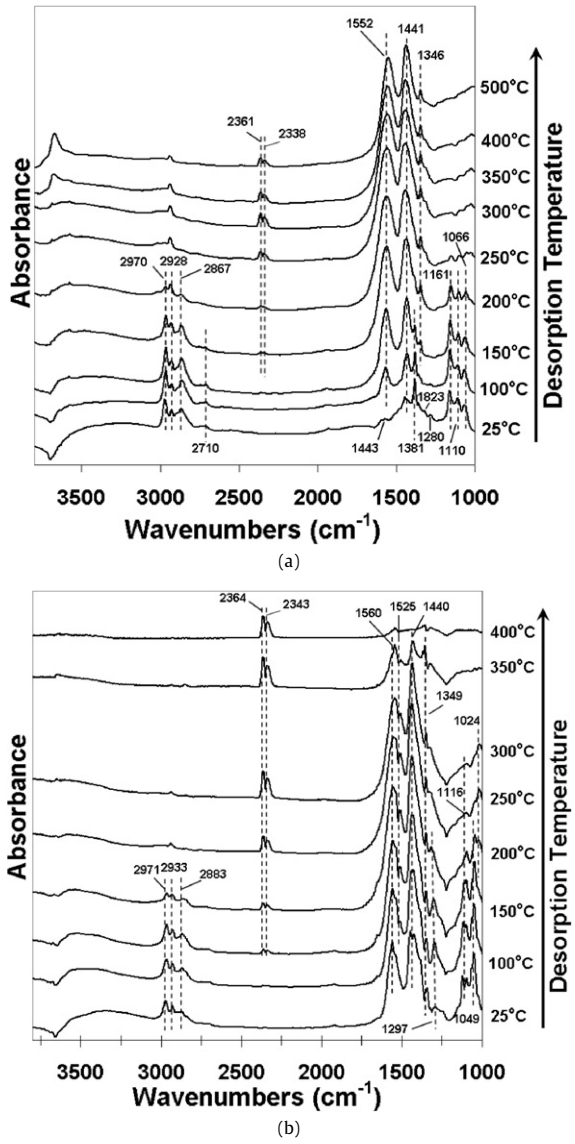

Fig. 9. *In situ* DRIFTS over (a) 10%Co/ZrO_2 and (b) 10%Co/CeO_2 during ethanol TPD.

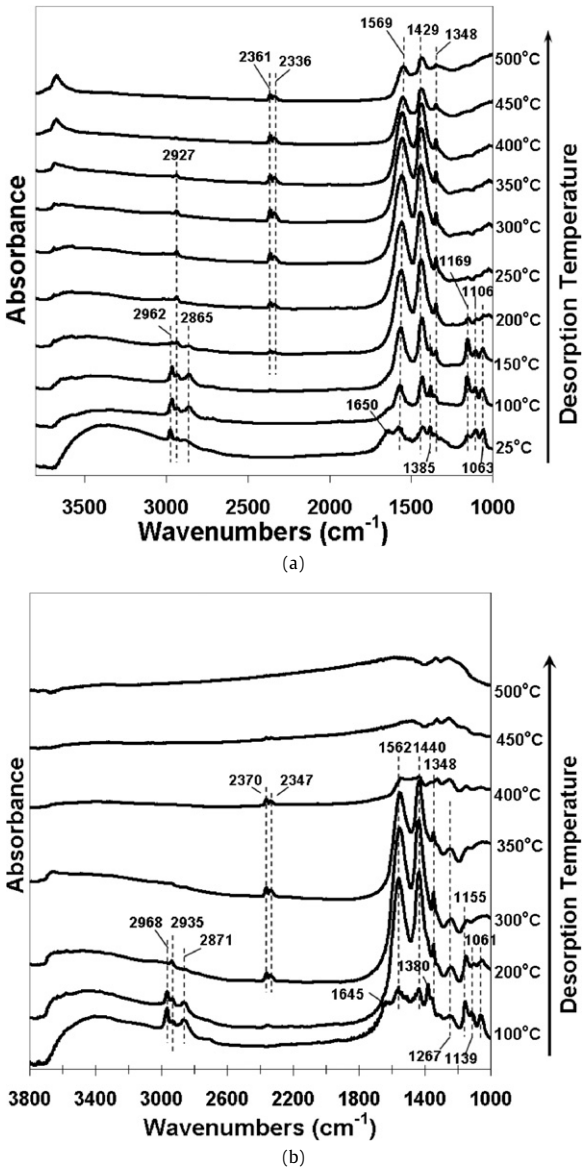

Fig. 10. *In situ* DRIFTS over (a) 10%Co/ZrO_2 and (b) 10%Co/10%CeO_2–ZrO_2 during ethanol/water TPD.

tion is apparent through the disappearance of acetate species at lower temperatures (Fig. 10b).

The oxygen storage characteristics of Co catalysts supported on ceria or zirconia and the bare supports were examined through O_2 pulse chemisorption. The samples were pre-reduced *in situ* prior to pulsing oxygen and monitoring oxygen uptake at 300 °C. The results are presented in Fig. 11. ZrO_2 support has no reducibility and shows no oxygen uptake. Ceria without any Co loading shows, although small, a non-negligible oxygen uptake, indicating modest reducibility. Partial reducibility of ceria near the surface at lower temperatures has been previously observed by other researchers [57,58]. Compared to blank supports, cobalt-loaded samples display much higher oxygen uptakes, however ceria-supported samples have a higher oxygen uptake compared to ZrO_2-supported ones, suggesting a greater accessibility of oxygen from the ceria lattice compared to zirconia. The difference between the oxygen uptake values is more pronounced when the Co-loaded samples is compared, suggesting a role for Co in facilitating oxygen mobility within the support. A similar phenomenon has been previously reported over noble-metal samples [59–62]. In fact, the quantification of the results shows that part of the oxygen uptake for the ceria-supported samples is attributable to the support.

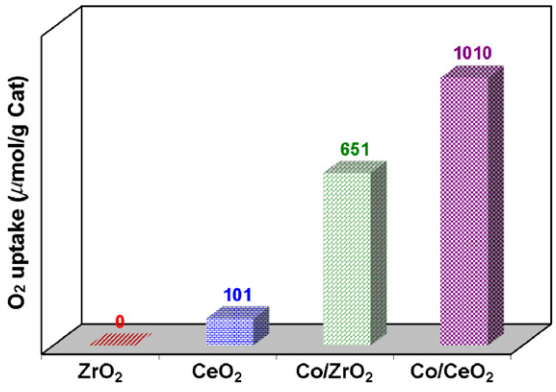

Fig. 11. Oxygen uptake during O_2 pulse chemisorption over ZrO_2, CeO_2, 10%Co/ZrO_2, and 10%Co/CeO_2.

Isotopic oxygen exchange technique has been widely accepted as a useful tool for investigating oxygen mobility in oxides [43–45]. The inset of Fig. 12a shows the typical profiles collected during

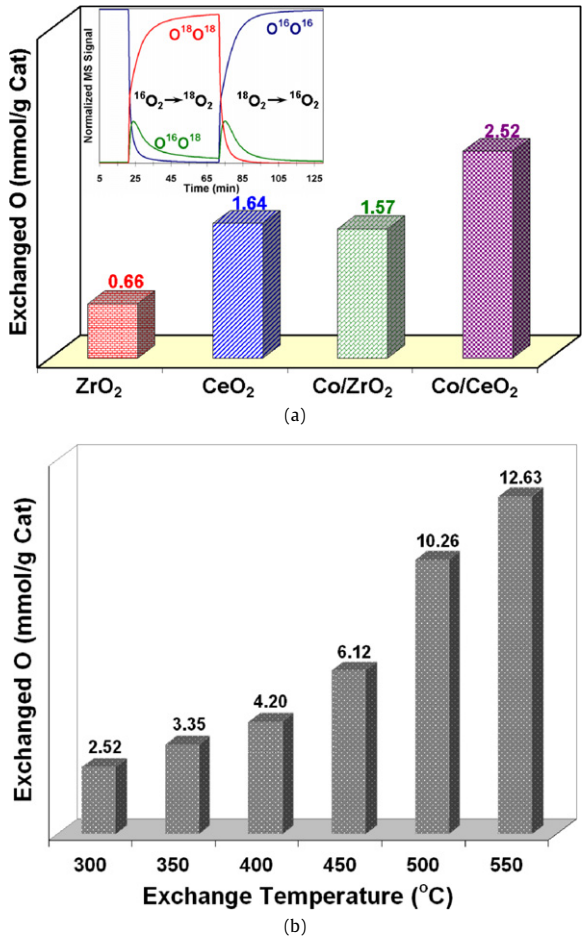

Fig. 12. (a) Oxygen exchange over ZrO_2, CeO_2, 10%Co/ZrO_2, and 10%Co/CeO_2 measured using $^{16}O_2/^{18}O_2$ switch and (b) Effect of temperature on oxygen exchange over 10%Co/CeO_2.

$^{16}O_2$-to-$^{18}O_2$ and $^{18}O_2$-to-$^{16}O_2$ switches. All the signals are normalized by the total counts. During the first switch, $^{16}O^{16}O$ signal ($m/z = 32$) decreases, accompanied by a rise of $^{18}O^{18}O$ signal ($m/z = 36$). The $^{16}O^{18}O$ signal ($m/z = 34$) is shown to go through a maximum. The $^{16}O^{18}O$ formation is derived from the dissociative adsorption of $^{18}O_2$ and subsequent recombination of the ^{18}O atom created and ^{16}O atom originally attached to the sample. This mechanism has been referred as going through a "three-atom complex" by Winter [63]. The doubly labeled oxygen results from a "four-atom" complex on the surface. Following the $^{18}O_2$-to-$^{16}O_2$ switch, relaxation and rise curves are essentially identical as well as the signal for the cross-labeled oxygen. After integrating the peak areas of corresponding oxygen species and subtracting the gas-phase holdup contribution determined from the Ar signal as described previously [56–58], the amount of exchanged oxygen atoms was calculated using a technique described previously in the literature [64] for the two bare supports and ceria- and zirconia-supported catalysts. As seen in Fig. 12a, not only the CeO_2 support, but also the CeO_2-supported Co sample presents notably higher oxygen mobility than their zirconia counterparts. The effect of the exchange temperature was further examined over Co–CeO_2 sample and shown in Fig. 12b. As expected, higher temperatures facilitate the lattice diffusion of oxygen atom, resulting in higher oxygen mobility. When the temperature reaches 550 °C, almost all of the oxygen atoms stored in the sample become accessible to participate in the exchange process.

When the results from different characterization experiments are combined, the emerging picture suggests that the availability of oxygen plays a key role in determining both the H_2 yield and the stability of the Co-based catalysts. Ethanol steam reforming can be considered as a redox reaction, where ethanol is oxidized by the oxygen species originating from water. If there is sufficient oxygen available/accessible, ethanol can be fully oxidized to CO_2. However, if replenishment of oxygen on the surface is slower compared to its depletion, other byproducts with intermediate oxidation states will be formed, including CH_4, carbon and CO. Hydrogen yield will be maximized when carbon in ethanol is oxidized all the way to CO_2. Therefore, effective delivery of oxygen to the oxidation sites plays a key role in determining the hydrogen yield and maintaining catalyst stability. Ethanol adsorbs preferentially on the Co sites and water molecules tend to adsorb onto support surface. The ethanol oxidation seems to take place at the interface of cobalt particles and the support. The higher oxygen mobility benefits the oxygen transfer across entire sample surface, resulting in complete oxidation of ethanol and in turn maximization of hydrogen production.

4. Conclusions

Steady-state reaction experiments coupled with post-reaction characterization experiments showed significant deactivation of Co/ZrO_2 catalysts through deposition of carbon on the surface, mostly in the form of carbon fibers, the growth of which is catalyzed by the Co particles. The addition of ceria appears to improve the catalyst stability due to its high OSC and high oxygen mobility, allowing gasification/oxidation of deposited carbon as soon as it forms. Although Co sintering is also observed, especially over the ZrO_2-supported catalysts, it does not appear to be the main mode of deactivation. The high oxygen mobility of the catalyst not only suppresses carbon deposition and helps maintain the active surface area, but it also allows delivery of oxygen to close proximity of ethoxy species, promoting complete oxidation of carbon to CO_2, resulting in higher hydrogen yields. Overall, oxygen accessibility of the catalyst plays a significant role on catalytic performance during BESR.

Acknowledgments

We gratefully acknowledge the funding from the US Department of Energy through the Grant DE-FG36-05GO15033.

References

[1] A. Erdőhelyi, J. Raskó, T. Kecskés, M. Tóth, M. Dömök, K. Baán, Catal. Today 116 (2006) 367–376.
[2] D.K. Liguras, D.I. Kondarides, X.E. Verykios, Appl. Catal. B 43 (2003) 345–354.
[3] J.R. Salge, G.A. Deluga, L.D. Schmidt, J. Catal. 235 (2005) 69–78.
[4] V. Fierro, O. Akdim, C. Mirodatos, Green Chem. 5 (2003) 20–24.
[5] A. Haryanto, S. Fernando, N. Murali, S. Adhikari, Energy Fuels 19 (2005) 2098–2106.
[6] P.D. Vaidya, A.E. Rodrigues, Chem. Eng. J. 117 (2006) 39–49.
[7] S. Cavallaro, V. Chiodo, S. Freni, N. Mondello, F. Frusteri, Appl. Catal. A 249 (2003) 119–128.
[8] C. Diagne, H. Idriss, A. Kiennemann, Catal. Commun. 3 (2002) 565–571.
[9] S. Cavallaro, Energy Fuels 14 (2000) 1195–1199.
[10] J.R. Mielenz, Curr. Opin. Microbiol. 4 (2001) 324–329.
[11] J. Llorca, P.R. de la Piscina, J.-A. Dalmon, J. Sales, N. Homs, Appl. Catal. B 43 (2003) 355–369.
[12] J. Llorca, N. Homs, J. Sales, P.R. de la Piscina, J. Catal. 209 (2002) 306–317.
[13] E.C. Wanat, K. Venkataraman, L.D. Schmidt, Appl. Catal. A 276 (2004) 155–162.
[14] T. Montini, L.D. Rogatis, V. Gombac, P. Fornasiero, M. Graziani, Appl. Catal. B 71 (2007) 125–134.
[15] J.R. Hansen, C.H. Christensen, J. Sehested, S. Helveg, J.R.R. Nielsen, S. Dahl, Green Chem. 9 (2007) 1016–1021.
[16] B.C. Zhang, X.L. Tang, Y. Li, W.J. Cai, Y.D. Xu, W.J. Shen, Catal. Commun. 7 (2006) 367–372.
[17] A.L. Alberton, M.M. Souza, M. Schmal, Catal. Today 123 (2007) 257–263.
[18] M.C. Sánchez, R.M. Navarro, J.L.G. Fierro, Int. J. Hydrogen Energy 32 (2007) 1462–1471.

[19] M.N. Barroso, M.F. Gomez, L.A. Arrúa, M.C. Abello, Appl. Catal. A 304 (2006) 116–123.
[20] F. Frusteri, S. Freni, V. Chiodo, L. Spadaro, G. Bonura, S. Cavallaro, J. Power Sources 132 (2004) 139–144.
[21] H.V. Fajardo, F.L.D. Probst, Appl. Catal. A 306 (2006) 134–141.
[22] A.N. Fatsikostas, D.I. Kondarides, X.E. Verykios, Catal. Today 75 (2002) 145–155.
[23] S. Freni, S. Cavallaro, N. Mondello, L. Spadaro, F. Frusteri, J. Power Sources 108 (2002) 53–57.
[24] A.J. Akande, R.O. Idem, A.K. Dalai, Appl. Catal. A. 287 (2005) 159–175.
[25] H. Wang, J.L. Ye, Y. Liu, Y.D. Li, Y.N. Qin, Catal. Today 129 (2007) 305–312.
[26] S. Tuti, F. Pepe, Catal. Lett. 122 (2008) 196–203.
[27] S.S.Y. Lin, D.H. Kim, S.Y. Ha, Catal. Lett. (2008) 295–301.
[28] J. Llorca, N. Homs, J. Sales, J.L.G. Fierro, P.R. de la Piscina, J. Catal. 222 (2004) 470–480.
[29] J.M. Guil, N. Homs, J. Llorca, P.R. de la Piscina, J. Phys. Chem. B 109 (2005) 10813–10819.
[30] N. Homs, J. Llorca, P.R. de la Piscina, Catal. Today 116 (2006) 361–366.
[31] J. Llorca, J.A. Dalmon, P.R. de la Piscina, N. Homs, Appl. Catal. A 243 (2003) 261–269.
[32] J. Llorca, A. Casanovas, T. Trifonov, A. Rodríguez, R. Alcubilla, J. Catal. 255 (2008) 228–233.
[33] J.C. Vargas, S. Libs, A.C. Roger, A. Kiennemann, Catal. Today 107–108 (2005) 417–425.
[34] J.C. Vargas, S. Libs, A.C. Roger, A. Kiennemann, Chem. Eng. Trans. 4 (2004) 247.
[35] M. Virginie, M. Araque, A.C. Roger, J.C. Vargas, A. Kiennemann, Catal. Today 138 (2008) 21–27.
[36] S.M. Lima, I.O. Cruz, G. Jacobs, B.H. Davis, L.V. Mattos, F.B. Noronha, J. Catal. 257 (2008) 356–368.
[37] H.S. Roh, Y. Wang, D.L. King, Top. Catal. 49 (2008) 32–37.
[38] H. Song, L.Z. Zhang, U.S. Ozkan, Catal. Today (2007) 346–354.
[39] H. Song, L.Z. Zhang, U.S. Ozkan, Green Chem. 9 (2007) 686–694.
[40] A. Yee, S.J. Morrison, H. Idriss, J. Catal. 186 (1999) 279–295.
[41] L.V. Mattos, F.B. Noronha, J. Catal. 233 (2005) 453–463.
[42] N. Laosiripojana, S. Assabumrungrat, Appl. Catal. B 66 (2006) 29–39.
[43] S.A. Driscoll, U.S. Ozkan, J. Catal. 97 (1993) 11524–11529.
[44] U.S. Ozkan, Y. Cai, J. Catal. 149 (1994) 375–389.
[45] U.S. Ozkan, Y. Cai, M.W. Kumthekar, J. Catal. 149 (1994) 390–403.
[46] D. Pietrogiacomi, S. Tuti, M.C. Campa, V. Indovina, Appl. Catal. B 28 (2000) 43–54.
[47] K. Takanabe, K. Nagaoka, K. Nariai, K.-I. Aika, J. Catal. 230 (2005) 75–85.
[48] R. Riva, H. Miessner, R. Vitali, G.D. Piero, Appl. Catal. A 196 (2000) 111–123.
[49] A.A. Khassin, T.M. Yurieva, V.V. Kaichev, V.I. Bukhtiyarov, A.A. Budneva, E.A. Paukshtis, V.N. Parmon, J. Mol. Catal. A 175 (2001) 189–204.
[50] L.F. Liotta, G.D. Carlo, G. Pantaleo, A.M. Venezia, G. Deganello, Appl. Catal. B 66 (2006) 217–227.
[51] F.B. Noronha, C.A. Perez, M. Schmal, R. Frety, Phys. Chem. Chem. Phys. 1 (1999) 2861–2867.
[52] M. Haneda, Y. Kintaichi, N. Bion, H. Hamada, Appl. Catal. B 46 (2003) 473–482.
[53] F. Tuinstra, J.L. Koenig, J. Chem. Phys. 53 (1970) 1126.
[54] J. Raskó, M. Dömök, K. Baán, A. Erdöhelyi, Appl. Catal. A 299 (2006) 202–211.
[55] L.V. Mattos, F.B. Noronha, J. Catal. 233 (2005) 453–463.
[56] S.Yu. Venyaminov, F.G. Prendergast, Anal. Biochem. 248 (1997) 234–245.
[57] A. Trovarelli, Catal. Rev. Sci. Eng. 38 (1996) 439–445.
[58] W. Cai, B. Zhang, Y. Li, Y. Xu, W. Shen, Catal. Commun. 8 (2007) 1588–1594.
[59] A. Trovarelli, Catal. Rev. Sci. Eng. 38 (1996) 439.
[60] J. Mikulová, J. Barbier Jr, S. Rossignol, D. Mesnard, D. Duprez, C. Kappenstein, J. Catal. 251 (2007) 172–181.
[61] E.M. Sadovskaya, Y.A. Ivanova, L.G. Pinaeva, G. Grasso, T.G. Kuznetsova, A. van-Veen, V.A. Sadykov, C. Mirodatos, J. Phys. Chem. A 111 (2007) 4498–4505.
[62] W. Cai, F. Wang, E. Zhan, A.C. Van Veen, C. Mirodatos, W. Shen, J. Catal. 257 (2008) 96–107.
[63] E.R.S. Winter, J. Chem. Soc. A 2889 (1968).
[64] J.S.J. Hargreaves, S.D. Jackson, G. Webb, Imprerial College Press, 2006, pp. 115–130.